CHINESE OPTICS LETTERS

Vol. 21, No. 12 | December 2023

Tissue optical clearing imaging for structural changes of neuromuscular junctions after mice ischemic stroke [Invited]

Jianyi Xu (徐健壹)†, Yi Dai (戴 奕)†, Ang Xuan (宣 昂)†, Yingtao Yao (姚应涛), Shaojun Liu (刘少军), Tingting Yu (俞婷婷), and Dan Zhu (朱 苒)*

Britton Chance Center for Biomedical Photonics, MoE Key Laboratory for Biomedical Photonics, Wuhan National Laboratory for Optoelectronics, Advanced Biomedical Imaging Facility, Huazhong University of Science and Technology, Wuhan 430074, China

*Corresponding author: dawnzh@mail.hust.edu.cn

Received September 3, 2023 | Accepted November 15, 2023 | Posted Online December 15, 2023

Ischemic stroke causes long-term disability and results in motor impairments. Such impairments are associated with structural changes in the neuromuscular junction (NMJ), including detailed morphology and three-dimensional (3D) distribution. However, previous studies only explored morphological changes of individual NMJs after stroke, which limits the understanding of their role in post-stroke motor impairment. Here, we examine 3D distributions and detailed morphology of NMJs in entire mouse muscles after unilateral and bilateral strokes induced by photothrombosis. The results show that 3D distributions and numbers of NMJs do not change after stroke, and severe unilateral stroke causes similar levels of NMJ fragmentation and area enlargement to bilateral stroke. This research provides structural data, deepening the understanding of neuromuscular pathophysiology after stroke.

Keywords: tissue optical clearing; optical imaging; stroke; neuromuscular junction.
DOI: 10.3788/COL202321.120061

1. Introduction

Stroke is the second leading cause of death and a major contributor to disability worldwide, impacting more than half of survivors, decreasing their quality of life, and causing significant social and economic challenges[1–3]. The disruption and protection of central neural circuits after stroke have received extensive attention[4–6]. Motor function requires not only precise control of the central nervous system (CNS) but also the integrity of structure and function in peripheral effectors. In recent years, researchers have moved beyond the CNS and begun to focus on the lesions and treatment of the peripheral nerve and skeletal muscle[7,8].

The neuromuscular junction (NMJ) is a synaptic structure in skeletal muscle that connects muscle fibers to spinal motor neurons and plays a crucial role in motor function[9,10]. Previous studies have demonstrated that stroke causes pathologic changes in skeletal muscles and NMJs[11–14]. Estrada-Bonilla *et al.* utilized nonspecific esterase techniques to reveal an increase in the NMJ area poststroke[14], while Balch's work also revealed that fragmentation of the NMJ occurred after a stroke within 21 days[13]. However, these results only showed the detailed morphological changes of individual NMJs after stroke. Local structural information does not accurately reflect the state of NMJs in overall skeletal muscle. Previous research has revealed that the 3D distribution and number of NMJs also determine the motor function of the muscle in addition to the morphological integrity of NMJs[15]. Thus, the lack of 3D structural information on NMJs in the whole muscle limits our understanding of their role in motor impairment after stroke.

The emergence of tissue optical clearing technology provides a new perspective for 3D imaging of large-volume tissues[16–19]. Recent advances in tissue clearing and optical imaging have allowed analysis of the morphology and distribution of NMJs in intact skeletal muscle[15,20,21], providing a novel approach to investigating the effects of stroke on NMJs. In this study, a targeted stroke model of the motor cortex was established through the combination of optical clearing skull window and photothrombosis. Motor function was evaluated using behavioral testing. The 3D distribution and detailed structural alterations of the NMJs during motor impairment were then examined using tissue clearing, confocal, and light-sheet microscopy following unilateral and bilateral motor cortex strokes.

2. Materials and Methods

2.1. Cerebral ischemia induced by photothrombosis

2.1.1. Animals

Thy1-YFP-16 (8–12 weeks old, male) mice were used in this study. Animals were housed on a 12 h/12 h light/dark cycle with access to food and water in a specific pathogen-free animal house. All animal care and experimental protocols were performed by the Experimental Animal Management Ordinance of Hubei Province, China, and the guidelines of Huazhong University of Science and Technology and were approved by the Institutional Animal Ethics Committee of Huazhong University of Science and Technology.

Cerebral ischemia was triggered via a photothrombosis technique combined with skull optical clearing[22,23].

2.1.2. Skull optical clearing

Mice were anesthetized with a mixture of 2% α-chloralose and 10% urethane (8 mL/kg) through intraperitoneal injection before the removal of their scalp to expose their skulls and holder attachment. The skulls (around 150 μm thick) were then treated with urea (10023218, Sinopharm) solution (S1) in 75% ethanol for 10 min and then with high-concentration SDBS (D166550, Sinopharm) solution (S2) for 5 min[24].

2.1.3. Photothrombosis

After establishing skull optical clearing, 0.2% rose bengal (RB) was injected into mice via the tail vein (0.4 mL/100 g; RB, 330000, Sigma-Aldrich). A 532 nm laser (7 mW/mm^2, Changchun New Industry Optoelectronics, China) was then used on the motor cortex to induce cerebral ischemia. Different trial groups included a nonirradiated sham group, a 30-s irradiated or 5-min irradiated unilateral stroke group, and a group where a secondary stroke was induced contralaterally two weeks after a 5-min irradiated unilateral stroke.

2.2. Assessment of motor function by behavioral test after stroke

2.2.1. Rotarod test

The rotarod test is one of the most widely used tests for assessing coordinated movements and balance of limbs in mice. To stay on the continuously accelerating rotarod, mice need to constantly adjust their positions to maintain their body balance. Mice would fall when they were incapable of keeping up with the rotarod. The time that mice were able to maintain their balance on this rod was recorded.

2.2.2. Grid walking test

The grid walking test is used to assess the coordination and fine function of mice. In brief, mice were placed on a wire grid and walked freely to measure the probability of stepping on the air and wrong position.

2.3. Preparation of brain section and skeletal muscle

2.3.1. Labeling NMJs

To label NMJ, Alexa Fluor 647 α-bungarotoxin (0.3 μg/g, α-BTX 647, Thermo Fisher Scientific, B35450) was injected via the tail vein for mice. After injecting fluorescent α-BTX with a 2 h conjugation time, the mice were perfused transcardially.

2.3.2. Sample dissection

Mice were anesthetized using a mixture of 2% α-chloralose and 10% urethane (0.8 mL/100 g, intraperitoneal), followed by transcardial perfusion with ice-cold 0.01 mol/L phosphate-buffered saline (PBS, P3813, Sigma-Aldrich) for 5–10 min. Subsequent perfusion with 4% (mass-to-volume ratio) paraformaldehyde (PFA, 158127, Sigma-Aldrich) in PBS was conducted for 10–20 min. For postperfusion, brain and muscle tissues were fixed in 4% PFA at 4°C for 24 h and repeatedly rinsed with PBS. Brain sections (100-μm-thick) were acquired using a Leica VT1000 S vibratome.

2.3.3. Immunostaining

For analysis of the infarct volume, brain sections were incubated with rabbit anti-NeuN primary antibody solution (Abcam, Ab177487, 1:500) at 4°C after incubation in the blocking solution. After washes in PBS, secondary incubation was conducted with Alexa Fluor 555 goat anti-rabbit (Thermo Fisher Scientific, A27039, 1:500) followed by more washes. The sections were then mounted on glass slides with 50% glycerol.

2.3.4. Muscle clearing

Tissues were dehydrated with tetrahydrofuran (THF, Sigma-Aldrich, 186562) solution at a series of concentrations (50, 70, 80, 100, 100, 100 volume-to-volume ratios, in dH_20, pH adjusted to 9.0 with triethylamine). Each step took 1–2 h, depending on the muscle thickness [approximately 1000–1300 μm for flexor digitorum profundus (FDP) and extensor digitorum longus (EDL)] and was performed at 4°C with gentle shaking. Thereafter, tissues were incubated in dibenzyl ether (DBE, Sigma-Aldrich, 108014) for refractive index matching[19].

2.4. Imaging

2.4.1. Laser speckle contrast imaging

Dynamical cerebral blood flow velocity was monitored by a home-built laser speckle contrast imaging (LSCI) system. A He–Ne laser (632.8 nm, 3 mW), diffused through a collimating beam mirror, illuminated the target imaging area. The backscattered light, after stereomicroscopic capture (SZX7, Olympus, Japan), was recorded via a camera (Pixelfly, PCO, Germany) at 40 frames and 20 ms exposure onto a computer. The original

scattered images were processed through temporal contrast analysis to obtain blood flow distribution.

2.4.2. Confocal microscopy

Imaging of NMJ structures was performed using a Zeiss LSM710 confocal microscope, employing a Fluar 10×/0.5 objective for full muscle, and an alpha 63×/1.46 objective for detailed NMJ evaluations.

2.4.3. Light-sheet fluorescence microscopy

Cleared muscles were imaged with light-sheet fluorescence microscopy (LiTone XL, Light Innovation Technology, Hong Kong, China), equipped with a 4× objective. For Thy1-YFP-16 mice labeled with α-BTX 647, 488 nm and 647 nm were used as exciting wavelengths. For intact muscle, the z-step interval was 5 μm.

2.5. Data processing and quantification

2.5.1. Infarct volume

Slices at 500 μm intervals underwent immunostaining and confocal imaging of neuronal nuclei. Fluorescent images of these slices were analyzed with ImageJ software. Impaired brain areas were identified and measured, aiding in stroke damage estimation. Damage volume was computed [damage-volume = Σ(damage-area × 500 μm)], and temporal trends of stroke damage area were evaluated.

2.5.2. NMJ number

Fluorescent images of intact skeletal muscle were analyzed with Imaris software. Automated calculations and segmentation were adjusted manually to incorporate unrecognized signal points and eliminate false data originating from residual bubbles post-clearing and autofluorescence in muscle fibers and blood vessels.

2.5.3. NMJ fragmentation

With Imaris software, an image stack was reconstructed and conducted to manually determine NMJ fragmentation. The YFP fluorescence signal marked the NMJ's origin, while the α-BTX (Alexa Fluor-647) fluorescence signal was used to visualize NMJ continuity. The combination of the fluorescence signals enables an accurate determination of the fragmentation level of each NMJ.

2.5.4. NMJ area

The structure of NMJ was visualized through a z-maximum projection by ImageJ. Individual NMJs were outlined utilizing the "Polygon selections" function, and their areas were quantified using "Analyze-Measure." For analysis, NMJs with a visible "pretzel" shape and aligned on the x–y plane were primarily selected.

2.5.5. Statistical analysis

Data analysis was performed using SPSS (IBM, USA). After assessing the normality of data distribution, the heterogeneity of variance was evaluated, and the one-way ANOVA was used to calculate P values. If the variance was homogeneous, we used the Bonferroni post hoc test for comparison; otherwise, we used Dunnett's T3 post hoc test for comparison. In this study, $P < 0.05$ was considered significant ($^{*}P < 0.05$, $^{**}P < 0.01$, and $^{***}P < 0.001$).

3. Results

3.1. Construction and evaluation of a unilateral stroke model

The impact of ischemic stroke on NMJ structure was investigated via photothrombosis-induced stroke in mice. Figure 1(a) illustrates the complete experiment process. After optical window creation and rose bengal injection, variable cerebral infarction was induced by differing laser exposure durations. The LSCI was used to monitor the change of the blood flow velocity to reflect the infarct of blood vessel after photothrombosis. The result showed a notable decline in blood flow velocity of the cortex post 5 min after irradiation, indicating that the infarct was induced successfully. Figure 1(b) showed the white-light images of the skull before and after skull clearing. Then the extent and

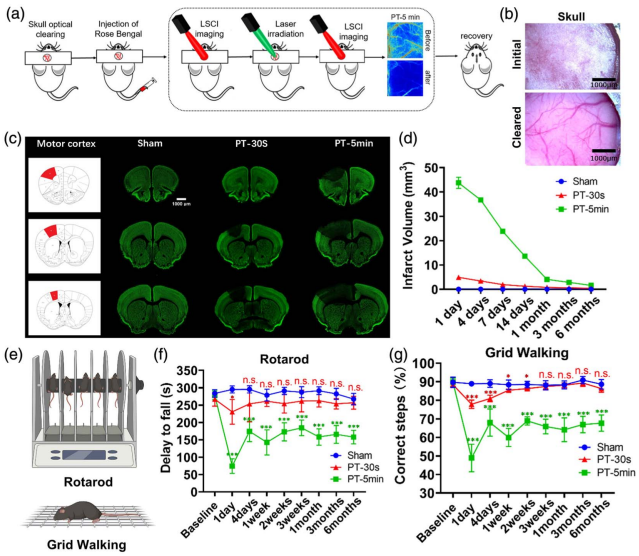

Fig. 1. Construction and evaluation of a unilateral stroke model. (a) Workflow for inducing ischemic stroke; (b) white-light images of the skull before and after skull optical clearing; (c) fluorescence imaging of the brain in the coronal sections from Sham, PT-30 s, and PT-5 min group; the red area on the left shows the motor cortex. (d) Quantification of the infarct volume of the brain ($n = 3$ at each time point). (e) Schematic diagrams of the rotarod test and the grid-walking test; (f), (g) scores for the rotarod test and grid walking at each time point after stroke in the sham group, PT-30 s group, and PT-5 min group ($n = 4$ for each behavior test).

location of the infarct were quantitatively determined using brain slices tagged with anti-NeuN antibodies [Fig. 1(c)]. The PT-5 min group exhibited more pronounced motor cortex damage and infarct volume than the PT-30 s group. Additionally, over time, both groups demonstrated a progressive decrease in infarct volume caused by the atrophy of the infarcted region [Fig. 1(d)].

Rotarod and grid-walking assessments revealed motor performance deficits in mice poststroke at different time points [Fig. 1(e)]. In contrast to the sham group, which exhibited consistent behavioral patterns before and after surgery, unaffected by rose bengal injection and skull optical clearing window creation, the PT-30 s and PT-5 min groups demonstrated significant but distinct impairments [Figs. 1(f) and 1(g)]. Specifically, the effects of irradiation lasting 30 s were found to be reversible, whereas exposure for 5 min resulted in irreversible motor impairment.

3.2. 3D visualization of NMJs in different muscles after stroke

The process of 3D visualization of NMJ distributions in intact skeletal muscles is shown in Fig. 2(a). To label NMJs, fluorescent α-BTX was injected via the tail vein of Thy1-YFP-16 mice. Subsequently, skeletal muscle was harvested after being transcardially perfused and performed with the FDISCO tissue clearing method. The cleared sample was mounted and then imaged with light-sheet microscopy. Imaris software was utilized to reconstruct and analyze the 3D distribution of NMJs in intact skeletal muscle.

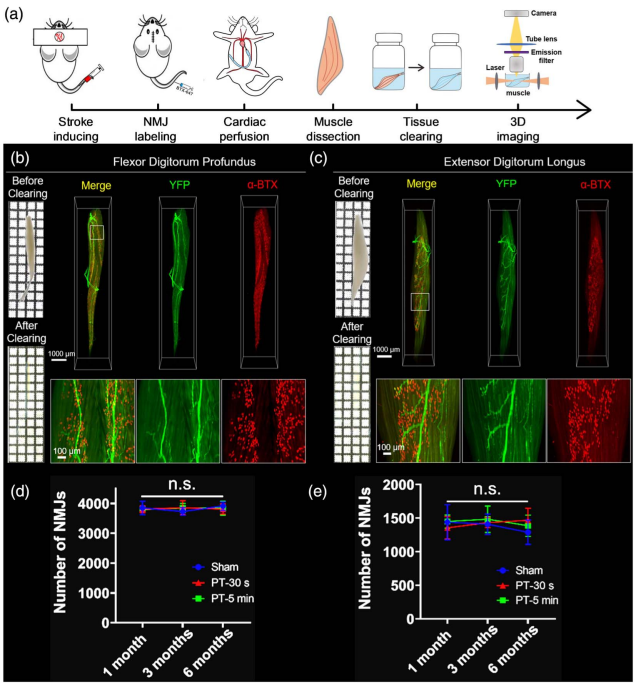

Fig. 2. 3D visualization and quantification of NMJs in different muscles after unilateral stroke. (a) Experimental pipeline for 3D visualization of NMJs and innervating nerves in skeletal muscles. (b), (c) 3D reconstructions of NMJs and innervating nerves in FDP and EDL; the images in the first row are enlarged and present in the second row. (d), (e) Quantification of NMJ numbers at each time point after stroke in different groups ($n = 3$ for each muscle at each time point); all values are presented as the mean ± SEM; statistical significance in (d) and (e) (n.s. represents not significant).

Figures 2(b) and 2(c) illustrate the distinctive 3D distribution features of the NMJs (α-BTX) and innervating nerves (YFP) in the EDL and FDP muscles. The distribution of NMJs within the FDP muscle reveals complexity, with bifurcated regions displaying different shapes: an inverted "V" shape in the upper region and a "spindle-shaped" structure in the lower. In the EDL muscle, NMJs are concentrated in the center, leading to a feather-like distribution. Subsequently, a detailed analysis of the NMJ number at each time point after stroke was performed. As shown in Figs. 2(d) and 2(e), there were no significant differences in the number of NMJs between each group. The number of NMJs showed no change at different time points. Thereafter, both 30 s and 5 min irradiation-induced strokes impart negligible effect on the numerical status of NMJs in the skeletal muscle.

3.3. Changes in the fine structure of NMJs after unilateral stroke

We focused on the fine structural changes of individual NMJs in different muscles by a combination of tissue clearing and confocal microscopy. As demonstrated in Fig. 3(a), a healthy NMJ (sham group) appears as a complete structure similar to a pretzel. In the PT-5 min group, although the NMJs maintained their pretzel-like shape after a stroke, they disintegrated into smaller fragments and spread out to the surrounding area.

Furthermore, the morphological features of the fine structure of the NMJs at different time points following the stroke were further quantitatively analyzed. For the extent of NMJ fragmentation, the NMJs in the sham group were primarily made up of either one or two fragments and remained steady for 6 months [Figs. 3(b) and 3(c)]. In the PT-30 s group, the number of fragments was not significantly different compared to the sham group [Fig. 3(c)]. And in the PT-5 min group, the number of fragments was significantly greater compared to the sham group, which shows that the degree of NMJ fragmentation increased gradually over time following the stroke.

The area changes of NMJs at different time points after the stroke are shown in Figs. 3(d) and 3(e). In the sham group, the area of the healthy NMJ increased with age progression. In the PT-30 s group, the NMJ area was not significantly different compared to the sham group. For the PT-5 min group, the area of NMJ in both muscles at 3 months after stroke was larger than the sham group's NMJ area, but at a six-month stroke survival period, there was an insignificant difference in the NMJ area across the entire group, suggesting a potential recovery or compensatory physiological mechanism.

Finally, we analyzed the proportion of NMJs with different levels of fragmentation after stroke. The results [Figs. 3(f) and 3(g)] showed that, in the sham and PT-30 s groups, more than

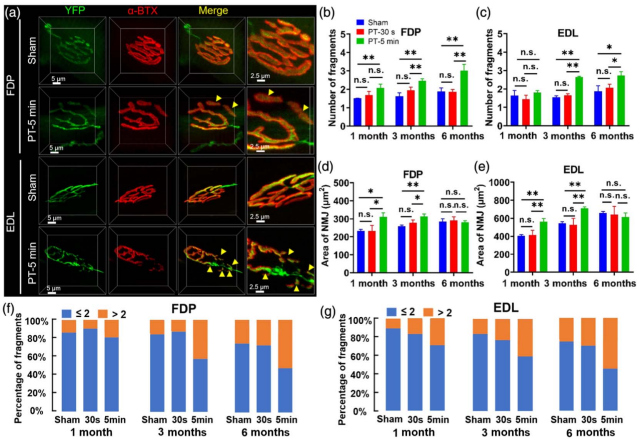

Fig. 3. Quantification of fine structural features of NMJs after unilateral stroke. (a) Comparison of the fine structure of NMJ in muscle after stroke, where the arrows point to the fragments; (b), (c) quantification of the number of fragments of NMJs at each time point after stroke in different groups in FDP and EDL muscles; (d), (e) quantification of NMJ area after stroke in different groups in FDP and EDL muscles; (f), (g) proportion of NMJs with different levels of fragmentation in FDP and EDL muscles after stroke; in FDP and EDL muscles, 562 and 635 NMJs were analyzed, respectively. "≤2" indicates the number of NMJ fragments is less than or equal to 2, representing "normal state;" ">2" indicates the number of NMJ fragments is greater than 2, representing "fragmentation." All values are presented as the mean ± SEM; $n = 3$ for each muscle at each time point; statistical significance in (b)–(e) (n.s. represents not significant, $^{*}P < 0.1$ and $^{**}P < 0.01$).

70% of NMJs can remain in a normal state (fragmented number ≤ 2). And in the PT-5 min group, the proportion of fragmented NMJs (fragmented number > 2) increases gradually following stroke, reaching almost 50% at 6 months after stroke.

The above results suggested that the PT-30 s stroke had no notable impact on NMJ structure, while the PT-5 min stroke disrupted the morphological structure of the NMJ, causing fragmentation and an increase in the NMJ area.

3.4. Changes in 3D distribution and fine structure of the NMJs after bilateral stroke

We established a bilateral stroke model (biPT-5 min group) that inhibits contralateral compensatory repair of the lesion and investigated the effects on NMJ structure after more severe injury. Mice were irradiated for 5 min after rose bengal injection to induce ischemic stroke in the right motor cortex [Fig. 4(a)]. Then, 14 days after the first stroke, a second stroke was induced in the left motor cortex. Rotarod and grid-walking tests (right limb only) were used to determine the effect of bilateral stroke on motor function at different time points.

The mice performed significantly worse in the rotarod test after the second stroke compared to the first stroke [Fig. 4(b)], indicating that bilateral stroke significantly impairs limb coordination. For the grid-walking test, the first stroke had little effect on the motor function of the right limb, with pronounced impairment only after the second stroke [Fig. 4(c)].

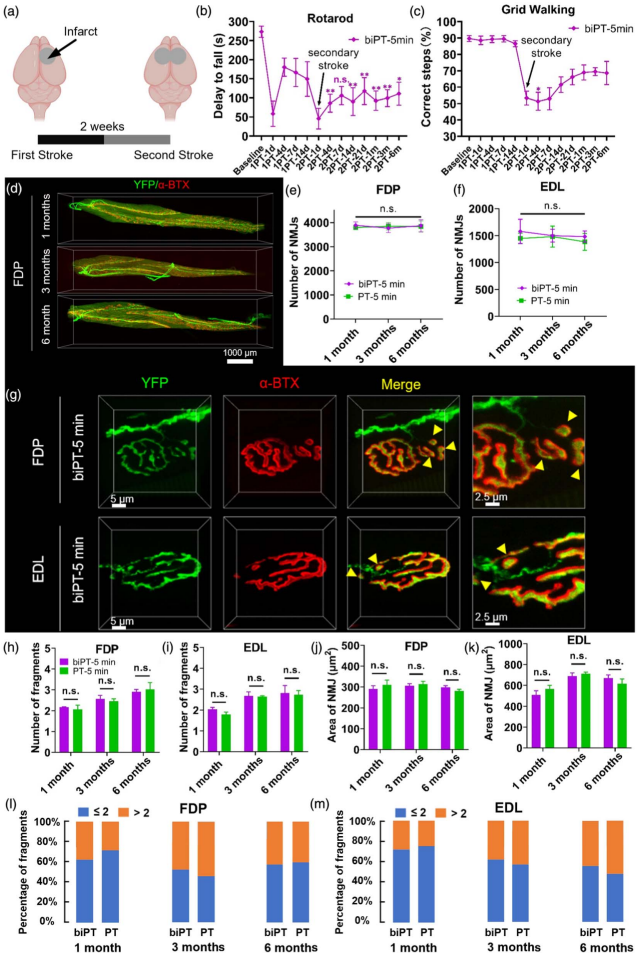

Fig. 4. 3D visualization and quantification of NMJs in different muscles after bilateral stroke. (a) Schematic diagram of the bilateral stroke model; (b), (c) scores for rotarod and grid walking at each time point ($n = 4$ at each time point); (d) 3D distributions of NMJs and innervating nerves in FDP muscles at different times; (e), (f) quantification of NMJ numbers in FDP and EDL muscles at each time point ($n = 3$ for each muscle at each time point); (g) fine structure of NMJs after bilateral stroke, where the arrows point to the fragments; (h), (i) quantification of the number of NMJ fragments in FDP and EDL muscles; (j), (k) quantification of the NMJ area in FDP and EDL muscles ($n = 3$ for each muscle at each time point); (l), (m) proportion of NMJs with different levels of fragmentation in FDP and EDL muscles after bilateral stroke; in the unilateral group, 190 and 218 NMJs in FDP and EDL muscles were analyzed; in the bilateral group, 175 and 158 NMJs in FDP and EDL muscles were analyzed. "≤2" indicates the number of NMJ fragments is less than or equal to 2, representing "normal state;" ">2" indicates the number of NMJ fragments is greater than 2, representing "fragmentation." All values are presented as the mean ± SEM; statistical significance in (b), (c), (e), (f), and (h)–(k) (n.s. represents not significant).

There was no significant difference observed between unilateral and bilateral strokes at most of the time points during the grid-walking test [Figs. 1(f) and 4(c)].

Then 3D distributions and numbers of NMJs in FDP and EDL following bilateral stroke were investigated. Taking the FDP muscle as an example, the distribution of NMJs and nerve branches within the FDP muscle throughout the time points

following bilateral stroke displayed a consistent 3D pattern [Fig. 4(d)]. Quantitative results of NMJ numbers in the FDP and EDL muscles revealed no significant difference between time points. Furthermore, no significant difference in NMJ numbers was observed between bilateral and unilateral strokes at the same time point [Figs. 4(e) and 4(f)]. These results indicate that inhibiting the contralateral compensation did not significantly alter the distribution or number of NMJs in skeletal muscle.

We investigated the fine structural alterations in NMJs at each time point following the bilateral stroke [Fig. 4(g)]. Figures 4(h) and 4(i) illustrate that there was no significant difference in the number of fragments between the biPT-5 min and PT-5 min groups at different time points. Additionally, the NMJ area in the muscle increased gradually after the bilateral stroke, but this change was not significant when compared to the unilateral stroke group [Figs. 4(j) and 4(k)].

Finally, we analyzed the proportions of NMJs with different levels of fragmentation after the bilateral stroke and compared them with those of the unilateral stroke. The results [Figs. 4(l) and 4(m)] showed that there is a similar level of the proportions of fragmented NMJs between the unilateral and bilateral groups.

Based on the above results, it can be concluded that more severe stroke through inhibition of contralateral compensation does not exacerbate the effect on the NMJ structure.

4. Discussion

Numerous animal models have been established to induce ischemic stroke[25,26], such as the middle cerebral artery occlusion (MCAo), craniotomy, photothrombosis, embolic stroke, and endothelin-1 models. Each method has its advantages when coping with various experimental conditions. Out of these, the photothrombotic model exhibits a lower mortality rate and higher targeting efficiency, which are vital parameters for the precise induction of motor cortex ischemic stroke. However, because of the skull's high absorption and scattering, the photothrombotic model is typically combined with an open-skull window, thinned skull window, or optical clearing skull window[27,28]. Among these methods, the optical clearing skull window preserves the prestroke brain environment most effectively[22,23]. Through clearing processing, skull scattering and absorption can be considerably reduced[29], rendering the photothrombotic stroke model controllable and targetable. Therefore, in this study, we employed tissue-clearing-assisted photothrombotic techniques to induce ischemic stroke in the motor cortex.

Previous work has primarily examined CNS changes after ischemic stroke[11,30,31], while the structural information of NMJs after ischemic stroke was still obtained using two-dimensional slices due to the limitations of traditional histological methods[12-14,32]. As a result, it is uncertain whether stroke affects the 3D distribution characteristics of NMJs, which are widely distributed throughout skeletal muscle. This study identifies a reduced motor function in mice following a motor cortex stroke, yet these mice maintain regular activities. Interestingly, NMJ spatial distribution characteristics remain unchanged, possibly due to multi-level neuronal compensatory mechanisms that may slow down the stroke-induced injury to the mouse motor cortex and NMJs.

Another finding observed in this study is that stroke significantly alters NMJ morphology, fragmenting and broadening its postsynaptic footprint and losing its pretzel-like pattern. In the PT-5 min group, the NMJ area increased significantly from 1 to 3 months compared to the sham group, but there was no significant difference compared to the sham group at 6 months after stroke. This phenomenon may be attributed to the fact that, on one hand, in the sham group, the NMJ area increased consistently from 1 to 6 months, resulting in the disappearance of the difference between the PT-5 min group and the sham group in 6 months. On the other hand, the severity of NMJ fragmentation caused by the stroke gradually decreased during subsequent development, leading to a decline in the NMJ area in the 6 months.

We investigated alterations in the NMJ structure following bilateral stroke, which means the inhibition of the contralateral compensation. The findings showed no noteworthy differences in the distribution and NMJ number relative to unilateral stroke. Thus, it could be hypothesized that following unilateral stroke, the ability of contralateral compensation to maintain the NMJ structure is restricted. Moreover, in addition to contralateral compensation, there exist other compensations after stroke, such as axonal sprouting of neurons in cortical regions unaffected by stroke[33], axonal sprouting of motor neurons in the brainstem[34], and neuronal compensation in the spinal cord[6]. These compensatory effects within the CNS decelerate the impact on the 3D structural features of NMJs in distal joints. Moreover, apart from CNS neurological compensation after a stroke, NMJs are not "static" postmaturation and dynamically regulate patterns of motor neuron control[35], thus dampening the changes in NMJs caused by a stroke. The plasticity and stability of the NMJ are regulated by various proteins, including agrin/low-density lipoprotein receptor-related protein 4 (LRP4)/muscle-specific kinase (MuSK) signalling axis, downstream targets docking protein 7 (Dok7), and 43 kDa receptor-associated protein of the synapse (rapsyn). In addition, terminal Schwann cells (TSCs) also play an important role in synaptogenesis and NMJ regeneration. Thus, future research could investigate NMJ structure after stroke with a combination of NMJ protein markers and TSCs to provide references for NMJ pathology and treatment.

In conclusion, we induced an ischemic stroke in mice using photothrombosis and skull optical clearing techniques. Then we used a combination of tissue clearing and optical imaging to examine the 3D distribution and fine structure of NMJs in intact skeletal muscle after stroke. The results indicate that the stroke did not affect the 3D distribution characteristics of NMJs, while severe unilateral stroke resulted in fragmentation and area enlargement of NMJs. Compared to unilateral stroke, the NMJ structure was not further exacerbated by bilateral stroke, although it caused more severe trauma by inhibiting contralateral compensation and further reducing motor

coordination. These results provide structural data on NMJs after stroke from a 3D perspective and advance the basic understanding of the role of NMJ structure in poststroke.

Acknowledgement

This work was supported by the National Natural Science Foundation of China (No. 61860206009), the Key Research and Development Project of Hubei Province (No. 2022BCA023), and the Innovation Fund of WNLO. The authors also thank the Optical Bio-imaging Core Facility of WNLO-HUST for support with data acquisition.

†These authors contributed equally to this work.

References

1. B. C. Campbell, D. A. De Silva, M. R. Macleod, S. B. Coutts, L. H. Schwamm, S. M. Davis, and G. A. Donnan, "Ischaemic stroke," Nat. Rev. Dis. Primers **5**, 70 (2019).
2. W. J. Powers, "Acute ischemic stroke," New Engl. J. Med. **383**, 252 (2020).
3. C. Villepinte, A. Verma, C. Dimeglio, X. De Boissezon, and D. Gasq, "Responsiveness of kinematic and clinical measures of upper-limb motor function after stroke: a systematic review and meta-analysis," Ann. Phys. Rehabil. Med. **64**, 101366 (2021).
4. T. C. Harrison, G. Silasi, J. D. Boyd, and T. H. Murphy, "Displacement of sensory maps and disorganization of motor cortex after targeted stroke in mice," Stroke **44**, 2300 (2013).
5. M. L. Starkey, C. Bleul, B. Zörner, N. T. Lindau, T. Mueggler, M. Rudin, and M. E. Schwab, "Back seat driving: hindlimb corticospinal neurons assume forelimb control following ischaemic stroke," Brain **135**, 3265 (2012).
6. A. S. Wahl, W. Omlor, J. C. Rubio, J. L. Chen, H. Zheng, A. Schröter, M. Gullo, O. Weinmann, K. Kobayashi, F. Helmchen, and B. Ommer, "Neuronal repair asynchronous therapy restores motor control by rewiring of the rat corticospinal tract after stroke," Science **344**, 1250 (2014).
7. A. Myatich, A. Haque, C. Sole, and N. L. Banik, "Clemastine in remyelination and protection of neurons and skeletal muscle after spinal cord injury," Neural Regen. Res. **18**, 940 (2023).
8. X. Xu, Z. Talifu, C. J. Zhang, F. Gao, H. Ke, Y. Z. Pan, H. Gong, H. Y. Du, Y. Yu, Y. L. Jing, and L. J. Du, "Mechanism of skeletal muscle atrophy after spinal cord injury: a narrative review," Front. Nutr. **10**, 1099143 (2023).
9. L. Li, W. C. Xiong, and L. Mei, "Neuromuscular junction formation, aging, and disorders," Annu. Rev. Physiol. **80**, 159 (2018).
10. H. Darabid, A. P. Perez-Gonzalez, and R. Robitaille, "Neuromuscular synaptogenesis: coordinating partners with multiple functions," Nat. Rev. Neurosci. **15**, 703 (2014).
11. S. Tiedt, A. M. Buchan, M. Dichgans, I. Lizasoain, M. A. Moro, and E. H. Lo, "The neurovascular unit and systemic biology in stroke–implications for translation and treatment," Nat. Rev. Neurol. **18**, 597 (2022).
12. N. Jalal, J. M. Gracies, and M. Zidi, "Mechanical and microstructural changes of skeletal muscle following immobilization and/or stroke," Biomech. Model. Mechan. **19**, 61 (2020).
13. M. H. Balch, H. Harris, D. Chugh, S. Gnyawali, C. Rink, S. M. Nimjee, and W. D. Arnold, "Ischemic stroke-induced polyaxonal innervation at the neuromuscular junction is attenuated by robot-assisted mechanical therapy," Exp. Neurol. **343**, 113767 (2021).
14. Y. C. Estrada-Bonilla, P. A. Castro de Souza-Tomé, F. M. Faturi, R. Mendes-Zambetta, A. C. Lepesteur-Gianlorenço, G. Croti, T. A. Jones, and T. L. Russo, "Compensatory neuromuscular junction adaptations of forelimb muscles in focal cortical ischemia in rats," Brain Behav. **10**, e01472 (2020).
15. J. Xu, J. Zhu, Y. Li, Y. Yao, A. Xuan, D. Li, T. Yu, and D. Zhu, "Three-dimensional mapping reveals heterochronic development of the neuromuscular system in postnatal mouse skeletal muscles," Commun. Biol. **5**, 1200 (2022).
16. J. Zhu, X. Liu, J. Xu, Y. Deng, P. Wang, Z. Liu, Q. Yang, D. Li, T. Yu, and D. Zhu, "A versatile vessel casting method for fine mapping of vascular networks using a hydrogel-based lipophilic dye solution," Cell Reports Methods **3**, 100407 (2023).
17. J. Zhu, D. Li, T. Yu, and D. Zhu, "Optical angiography for diabetes-induced pathological changes in microvascular structure and function: an overview," J. Innov. Opt. Heal. Sci. **15**, 2230002 (2022).
18. H. Mai, J. Luo, L. Hoeher, R. Al-Maskari, I. Horvath, Y. Chen, F. Kofler, M. Piraud, J. C. Paetzold, J. Modamio, and M. Todorov, "Whole-body cellular mapping in mouse using standard IgG antibodies," Nat. Biotech., in press (2023).
19. Y. Qi, T. Yu, J. Xu, P. Wan, Y. Ma, J. Zhu, Y. Li, H. Gong, Q. Luo, and D. Zhu, "FDISCO: advanced solvent-based clearing method for imaging whole organs," Sci. Adv. **5**, eaau8355 (2019).
20. X. Yin, T. Yu, B. Chen, J. Xu, W. Chen, Y. Qi, P. Zhang, Y. Li, Y. Kou, Y. Ma, and N. Han, "Spatial distribution of motor endplates and its adaptive change in skeletal muscle," Theranostics **9**, 734 (2019).
21. S. C. Daeschler, J. Zhang, T. Gordon, and G. H. Borschel, "Optical tissue clearing enables rapid, precise and comprehensive assessment of three-dimensional morphology in experimental nerve regeneration research," Neural Regen. Res. **17**, 1348 (2022).
22. Z. Hu, D. Li, X. Zhong, Y. Li, A. Xuan, T. Yu, J. Zhu, and D. Zhu, "*In vivo* tissue optical clearing assisted through-skull targeted photothrombotic ischemic stroke model in mice," J. Biomed. Opt. **27**, 065001 (2022).
23. D. Li, L. Deng, Z. Hu, Y. Li, T. Yu, X. Zhong, J. Zhu, and D. Zhu, "Optical clearing imaging assisted evaluation of urokinase thrombolytic therapy on cerebral vessels with different sizes," Biomed. Opt. Express **13**, 3243 (2022).
24. C. Zhang, W. Feng, Y. Zhao, T. Yu, P. Li, T. Xu, Q. Luo, and D. Zhu, "A large, switchable optical clearing skull window for cerebrovascular imaging," Theranostics **8**, 2696 (2018).
25. M. Caleo, "Rehabilitation and plasticity following stroke: insights from rodent models," Neuroscience **311**, 180 (2015).
26. F. Fluri, M. K. Schuhmann, and C. Kleinschnitz, "Animal models of ischemic stroke and their application in clinical research," Drug Des. Dev. Ther. **9**, 3445 (2015).
27. Y. J. Zhao, T. T. Yu, C. Zhang, Z. Li, Q. M. Luo, T. H. Xu, and D. Zhu, "Skull optical clearing window for *in vivo* imaging of the mouse cortex at synaptic resolution," Light-Sci. Appl. **7**, 17153 (2018).
28. D. Li, Z. Hu, H. Zhang, Q. Yang, L. Zhu, Y. Liu, T. Yu, J. Zhu, J. Wu, J. He, and P. Fei, "A through-intact-skull (TIS) chronic window technique for cortical structure and function observation in mice," eLight **2**, 15 (2022).
29. Y. Zhang, C. Zhang, X. Zhong, and D. Zhu, "Quantitative evaluation of SOCS-induced optical clearing efficiency of skull," Quant. Imag. Med. Surg. **5**, 136 (2015).
30. M. T. Joy and S. T. Carmichael, "Encouraging an excitable brain state: mechanisms of brain repair in stroke," Nat. Rev. Neurosci. **22**, 38 (2021).
31. T. Shichita, H. Ooboshi, and A. Yoshimura, "Neuroimmune mechanisms and therapies mediating post-ischaemic brain injury and repair," Nat. Rev. Neurosci. **24**, 299 (2023).
32. M. J. Cullins, J. A. Russell, Z. E. Booth, and N. P. Connor, "Central activation deficits contribute to post stroke lingual weakness in a rat model," J. Appl. Physiol. **130**, 964 (2021).
33. T. H. Murphy and D. Corbett, "Plasticity during stroke recovery: from synapse to behaviour," Nat. Rev. Neurosci. **10**, 861 (2009).
34. L. C. Bachmann, N. T. Lindau, P. Felder, and M. E. Schwab, "Sprouting of brainstem-spinal tracts in response to unilateral motor cortex stroke in Mice," J. Neurosci. **34**, 3378 (2014).
35. R. T. Hepple and C. L. Rice, "Innervation and neuromuscular control in ageing skeletal muscle," J. Physiol. **594**, 1965 (2016).